

***Hubble Space Telescope WFC3 Early Release Science:
Emission-Line Galaxies from Infrared Grism Observations***

Amber N. Straughn^{1,2}, Harald Kuntschner³, Martin Kümmel³, Jeremy R. Walsh³, Seth H. Cohen⁴, Jonathan P. Gardner², Rogier A. Windhorst⁴, Robert W. O'Connell⁵, Norbert Pirzkal⁶, Gerhardt Meurer⁷, Patrick J. McCarthy⁸, Nimish P. Hathi⁹, Sangeeta Malhotra⁴, James Rhoads⁴, Bruce Balick⁹, Howard E. Bond⁶, Daniela Calzetti¹⁰, Michael J. Disney¹¹, Michael A. Dopita¹², Jay A. Frogel¹³, Donald N. B. Hall¹⁴, Jon A. Holtzman¹⁵, Randy A. Kimble², Max Mutchler⁶, Francesco Paresce¹⁶, Abhijit Saha¹⁷, Joseph I. Silk¹⁸, John T. Trauger¹⁹, Alistair R. Walker²⁰, Bradley C. Whitmore⁶, Erick T. Young²¹, Chun Xu²²

ABSTRACT

We present grism spectra of emission–line galaxies (ELGs) from 0.6–1.6 microns from the Wide Field Camera 3 (WFC3) on the Hubble Space Telescope (HST). These new infrared grism data augment previous optical Advanced Camera for Surveys G800L 0.6–0.95 micron grism data in GOODS–South from the PEARS program, extending the wavelength coverage well past the G800L red cutoff. The ERS grism field was observed at a depth of 2 orbits per grism, yielding

¹amber.n.straughn@nasa.gov

²Astrophysics Science Division, Goddard Space Flight Center, Code 665, Greenbelt, MD 20771

³Space Telescope European Coordinating Facility, Karl Schwarzschild Str. 2, D 85748 Garching, Germany

⁴School of Earth and Space Exploration, Arizona State University, Tempe, AZ 85287

⁵Department of Astronomy, University of Virginia, Charlottesville, VA 22904-4325

⁶Space Telescope Science Institute, Baltimore, MD 21218

⁷International Centre for Radio Astronomy Research, The University of Western Australia, Crawley WA, 6009

⁸Observatories of the Carnegie Institute of Washington, Pasadena, CA 91101

⁹Department of Physics & Astronomy, University of California, Riverside, CA 92521

⁹Department of Astronomy, University of Washington, Seattle, WA 98195-1580

¹⁰Department of Astronomy, University of Massachusetts, Amherst, MA 01003

¹¹School of Physics and Astronomy, Cardiff University, Cardiff CF24 3AA, United Kingdom

¹²Research School of Astronomy & Astrophysics, The Australian National University, ACT 2611, Australia

¹³Association of Universities for Research in Astronomy, Washington, DC 20005

¹⁴Institute for Astronomy, University of Hawaii, Honolulu, HI 96822

¹⁵Department of Astronomy, New Mexico State University, Las Cruces, NM 88003

¹⁶Istituto di Astrofisica Spaziale e Fisica Cosmica, INAF, Via Gobetti 101, 40129 Bologna, Italy

¹⁷National Optical Astronomy Observatories, Tucson, AZ 85726-6732

¹⁸Department of Physics, University of Oxford, Oxford OX1 3PU, United Kingdom

¹⁹NASA–Jet Propulsion Laboratory, Pasadena, CA 91109

²⁰Cerro Tololo Inter-American Observatory, La Serena, Chile

²¹NASA–Ames Research Center, Moffett Field, CA 94035

²²Shanghai Institute of Technical Physics, 200083 Shanghai, China

spectra of hundreds of faint objects, a subset of which are presented here. ELGs are studied via the $H\alpha$, [O III], and [O II] emission lines detected in the redshift ranges $0.2 \lesssim z \lesssim 1.4$, $1.2 \lesssim z \lesssim 2.2$ and $2.0 \lesssim z \lesssim 3.3$ respectively in the G102 (0.8–1.1 microns; $R \simeq 210$) and G141 (1.1–1.6 microns; $R \simeq 130$) grisms. The higher spectral resolution afforded by the WFC3 grisms also reveals emission lines not detectable with the G800L grism (e.g., [S II] and [S III] lines). From these relatively shallow observations, line luminosities, star-formation rates, and grism spectroscopic redshifts are determined for a total of 48 ELGs to $m_{AB(F098M)} \simeq 25$ mag. Seventeen GOODS-South galaxies that previously only had photometric redshifts now have new grism-spectroscopic redshifts, in some cases with large corrections to the photometric redshifts ($\Delta z \simeq 0.3$ – 0.5). Additionally, one galaxy had no previously-measured redshift but now has a secure grism-spectroscopic redshift, for a total of 18 new GOODS-South spectroscopic redshifts. The faintest source in our sample has a magnitude $m_{AB(F098M)} = 26.9$ mag. The ERS grism data also reflect the expected trend of lower specific star formation rates for the highest mass galaxies in the sample as a function of redshift, consistent with downsizing and discovered previously from large surveys. These results demonstrate the remarkable efficiency and capability of the WFC3 NIR grisms for measuring galaxy properties to faint magnitudes and redshifts to $z \gtrsim 2$.

Subject headings: catalogs — techniques: spectroscopic — galaxies: starburst

1. Introduction

Galaxies that are actively star-forming make up a distinct population of sources that are involved in ongoing evolution—that is, they are in the very process of converting gas into stars and thereby changing their chemical content and stellar mass. Star-forming galaxies are also often associated with larger scale galaxy evolution across cosmic time, in that galaxy interactions are often found to cause enhanced star formation (e.g., Li et al. 2008, Overzier et al. 2008, Larson & Tinsley 1978) and galaxy evolution as a whole is thought to proceed hierarchically via galaxy interactions and merging (e.g., White & Frenk 1991; Navarro et al. 1997, etc.). These actively star-forming galaxies are therefore important to study within the overall context of galaxy assembly. Information about star formation activity is revealed in the galaxies’ emission lines, particularly $H\alpha$, [O III], and [O II] at rest-frame wavelengths $\lambda 6563\text{\AA}$, $\lambda 4959\text{\AA}$, 5007\AA , and $\lambda 3727\text{\AA}$ respectively. Many studies have used emission lines to investigate the star-forming properties of galaxies over various redshift ranges (Hammer et al. 1997; Kennicutt 1983; Gallego et al. 1995; Kewley et al. 2004;

NICMOS grism study: McCarthy et al. 1999, Yan et al. 1999; WISP grism Survey: Atek et al. 2010).

The installation of the new Wide Field Camera 3 (WFC3) on the Hubble Space Telescope (HST) in mid–2009 has provided a new capability for studying star formation and has already resulted in a variety of scientific discoveries in observational cosmology. Particularly, the increase in sensitivity, field of view, and resolution of the WFC3/IR over previous infrared instrumentation has been used to detect some candidates for the most distant galaxies ever observed (Bouwens et al. 2010, Yan et al. 2010a, Oesch et al. 2010, McLure et al. 2010, Finkelstein et al. 2010) etc.) from the ultra–deep WFC3 imaging (Illingworth et al. PID GO–11563) of the Hubble Ultra Deep Field (HUDF; Beckwith et al. 2006). The less deep but wider–area broadband data from the Early Release Science (ERS) II (PI O’Connell, PID GO–11359) program have also been used to study high–redshift candidates (Wilkins et al. 2010, Labbe et al. 2010, Bouwens et al. 2010, Yan et al. 2010b) and UV–dropout galaxies (Hathi et al. 2010). Windhorst et al. (2010) describe the WFC3 ERS program in detail, which we summarize in Section 2.

In addition to the broadband data used for most of these studies, the ERS II program also consists of one field observed with both the G102 (0.8–1.1 microns; $R \simeq 210$) and G141 (1.1–1.6 microns; $R \simeq 130$) infrared grisms (described in detail below). van Dokkum et al. (2010) report on a bright $z=1.9$ compact galaxy in the ERS grism data. Here, we present emission–line galaxies from the WFC3 ERS grism observations, demonstrating the unique capability of this instrument for detecting star–forming galaxies in the infrared reaching to magnitudes $m_{AB(F098M)} \simeq 25$ mag with only 2 orbits of HST time. By searching for emission lines in the infrared grism data, we are able to push detection of these galaxies and subsequent measurement of their physical properties to redshifts $z \simeq 2.0$. Grism studies with HST’s Advanced Camera for Surveys (ACS) G800L grism have proven successful at detecting emission–line galaxies (ELGs) in the optical (Meurer et al. 2007, Straughn et al. 2008, Straughn et al. 2009, Xu et al. 2007, Pirzkal et al. 2006), and here we extend these studies of ELGs to the infrared.

2. Data

The ERS II program for WFC3 consists of both UV and IR observations of about 30% of the GOODS–South field (Giavalisco et al. 2004). Here we summarize the ERS II program; Windhorst et al. (2010) present the ERS II data reduction effort in detail. Eight pointings were imaged with the UVIS channel (UV filters F225W, F275W, and F336W at depths of 2 orbits/pointing/filter for F225W and F275W and 1 orbit/pointing for F336W) and ten

with the IR channel (filters F098M, F125W, F160W) at 2 orbits/pointing/filter. Grism observations of one WFC3 pointing (c.f. Fig. 1) were performed using the infrared “blue” G102 grism ($R \simeq 210$) and the “red” ($R \simeq 130$) G141 grism, providing spectral coverage from 0.8–1.6 microns at 2 orbits/grism depth.

The WFC3 IR channel has a field of view of 4.65 arcminutes² at a resolution of 0.19 arcsec/pixel. The ten 5 x 2 grid pattern WFC3/ERS II IR pointings span the northern $\simeq 40$ square arcminutes of GOODS–South, providing new high–resolution infrared imaging to accompany this widely–used multiwavelength dataset. The ERS II grism field lies in the north–central region of the ERS II imaging field (Fig. 1; J2000 53.071121 -27.709646) and is overlapped completely by the HST Probing Evolution And Reionization Spectroscopically (PEARS; Malhotra PID 10530) ACS grism survey South Field #4. As such, combined with the earlier ACS data, these new infrared grism data provide unprecedented spectral grism coverage in the optical to infrared wavelength range of objects reaching to continuum magnitude $m_{AB(F098M)} \simeq 25$ mag.

3. Analysis

The latest version (March 11, 2010) STSDAS *CALWF3* v2.0 pipeline reduced direct imaging and the associated grism exposures were obtained from the MAST Archive. The direct images were combined for each of the F098M and F140W filters using Multidrizzle (Koekemoer et al. 2002) and small shifts of up to 0.7 pixels were applied to individual images for alignment. Source catalogues were produced for each filter using SExtractor (Bertin & Arnouts 1996). The resulting catalogues were cleaned to remove spurious sources at the edges and artifacts from persistence effects caused by a bright star in the preceding ERS grism observations.

The final, cleaned source catalogues were used with the aXe grism reduction software (version 2.0; Kümmel et al. 2009) to extract a calibrated 2–dimensional, co–added grism spectrum for each source. Master sky backgrounds for each grism were constructed from all publicly available grism data as of February 2010 and subtracted from the ERS observations prior to spectral reduction. The final 2–dimensional grism spectra include information about the associated errors and contamination by spectra of neighboring objects. The trace and wavelength calibration used by aXe to extract the spectra was based on the first in–orbit calibration observations (Kuntschner et al. 2009a,b).

3.1. Source Selection

We visually examined all emission–line candidate sources located in the ERS grism field; many ELGs with prominent emission lines detected in PEARS with the G800L grism also have lines in the infrared. In addition to previously–detected PEARS ELGs, there are also sources in the field in which the strongest emission lines lie exclusively in the infrared and so were not detected in PEARS. We used standard Gaussian fitting techniques to measure emission line fluxes and calculate SFRs based on the line luminosities, as described in the following Section. ELGs that have line flux measurements with $S/N \geq 2$ are retained in the final catalog (Table 1); 83% of lines have $S/N \geq 3$. Whereas the PEARS pre–selected galaxies by definition have more than one line—and therefore line identifications based on the line wavelength ratio are unambiguous and in some cases already determined by the ACS grism spectra—a small number of ERS II ELG candidates only have one emission line. For these sources, spectroscopic and photometric redshift catalogs (Grazian et al. 2006; Wuyts et al. 2008; Balestra et al. 2010; Vanzella et al. 2008) are consulted in order to determine if the source has a previously–measured redshift. If it does, line identification is accomplished via this redshift and a grism–spectroscopic redshift (Cohen et al. 2010, in prep.; Xia et al. 2010) is calculated based on the line identification. If it does not, the line remains unidentified (see Table 1). However, 60% of the ELGs have two or more emission lines, and therefore it is straightforward to assign line identifications based on the emission line wavelength ratio. The fraction of objects with two lines in the spectra is considerably higher than in the PEARS studies (where the fraction of sources with two lines was $\simeq 30\%$) for two main reasons. First, the wavelength range for both the G102 and G141 is longer by a factor of more than 2; and second, the higher spectral resolution afforded by both WFC3 grisms allows detection of lines not previously seen in the G800L observations; namely, [S II] at $\lambda\lambda 6716+6731\text{\AA}$ is now sufficiently resolved from $H\alpha$ (Figure 2) and [S III] at $\lambda\lambda 9069, 9532\text{\AA}$ is detected in several sources as well. Additionally, the higher resolution allows in some cases $H\beta$ and the two [O III] lines at $\lambda 4959$ and $\lambda 5007$ to be detected ([O III] at $\lambda\lambda 4959, 5007$ can be marginally resolved in some cases; see Figure 3). This higher resolution allows, e.g., a line identification in the extremely faint (continuum) Object 397, which has no other significant line detections in the spectrum. Four objects in the sample are also X–ray sources and likely AGN (Szokoly et al. 2004); these are noted in Table 1.

4. Results

4.1. ERS II Emission–Line Galaxy Sample

Our final catalog of WFC3 ERS II ELGs contains 48 galaxies with a total of 73 emission lines. Of these, 29 are $H\alpha$, 27 [O III], 6 [O II], 2 [S II], 2 [S III] λ 9069, 2 [S III] λ 9532, and 5 unidentified lines (see Table 1). The average redshift of these galaxies is $z=1.200$ with a redshift range of $z=0.227$ – 2.315 (Figure 4). The galaxies’ broadband F098M magnitudes span $m_{AB(F098M)}=18.67$ – 26.87 mag with an average magnitude $m_{AB(F098M)}=23.65$ mag. The faintest continuum magnitude source is Object 103 ($m_{AB(F098M)}=26.87$ mag) at redshift $z=1.680$ with both [O II] and [O III] detected.

The ERS grism pointing lies completely within PEARS–South Field 4, and a total of 25 PEARS–detected ELGs fall into this field. Thirteen of these have emission lines in the G102/G141 bandpasses with fluxes meeting the $S/N \gtrsim 2$ requirement (see Figure 2 for example spectra). Many of these objects are sources with [O III] emission in the optical, and $H\alpha$ falling in the G102 grism bandpass. One such example is Object # 370 (PEARS Object # 119489; Straughn et al. 2009). This object is also a CDF–S X–ray source (Szokoly et al. 2004; Grogin et al. 2007), which was observed to have one strong line in the optical. We now detect another strong line in the infrared, making line identifications possible via the wavelength ratio (Figure 2). Several PEARS–detected galaxies have [O III] emission near the red edge of the G800L bandpass, which overlaps with the G102 grism, and so [O III] is observed in G102 as well. For these sources, $H\alpha$ falls into the lower–resolution G141 bandpass. Several other single–line PEARS ELGs also have emission lines detected in G102 and/or G141 and now have grism–spectroscopic redshifts, thus demonstrating the utility of the extended wavelength/redshift range compared to ACS G800L for identifying emission lines. Due to the higher resolution of the WFC3 grisms, the [O III] $\lambda\lambda 4959\text{\AA}$, 5007\AA lines are individually detectable (though not fully resolved) in these data (e.g., Fig. 3 Objects 402 and 397), whereas they are blended in the ACS G800L grism data. Also of note in this sample are the sources which have prominent emission lines in all three grism bandpasses—and thus different star–formation indicators.

In addition to PEARS–selected ELGs, other emission line sources were identified in the ERS II grism field that do not have lines detected in the optical G800L grism data. Thirty–five such sources that make the $S/N \gtrsim 2$ cut are listed in Table 1. Prevalent among these objects are ELGs with $H\alpha$ in the G102 bandpass; many of these also have [S III] detections in G141 (Fig. 2). A few of the WFC3–detected sources are $z \approx 2$ galaxies with [O II] and/or [O III] lines visible in the IR grism bandpasses (e.g., Objects 242 and 578 in Table 1). Grism redshifts (Figure 4) are derived for all sources as described in Section 3.1 and

are also presented in Table 1. Seventeen GOODS–South galaxies that previously only had photometric redshifts now have new grism–spectroscopic redshifts. Some of these objects have large corrections to the photometric redshifts ($\Delta z \simeq 0.3\text{--}0.5$). Additionally, one galaxy (Object 226) had no previously–measured redshift but now has a secure grism–spectroscopic redshift, for a total of 18 new spectroscopic redshifts. Two sources in our catalog (402 and 474; see Figure 3 for example) have published FORS2 and VIMOS spectroscopic redshifts (Vanzella et al. 2008; Balestra et al. 2010) that disagree with our measurements which are listed in Table 1.

4.2. Star Formation in ERS II ELGs

The longer wavelength range over which to detect emission lines provides more sources with multiple lines that can be used in calculating SFRs. In particular, $H\alpha$ —the emission line which yields the most direct and secure SFR estimate (e.g., Kennicutt 1998)—is now observed in 29 sources. Given the low resolution of the grism spectra, some contribution from [NII] $\lambda\lambda 6548, 6584$ will be present in the measured $H\alpha$ line fluxes due to the blending of the lines. The strength of this contribution in general galaxy samples varies from a few percent to factors of 0.3–0.5 for particularly massive and metal–rich galaxies (Jansen et al. 2000, Gallego et al. 1997, Kennicutt et al. 1992). Because of this wide variation owing to differences in effective temperature, ionization, and metallicity, we do not adopt a global [NII] correction and instead note that the $H\alpha$ fluxes presented here are likely overestimates. For each of the ELGs, we calculate SFRs via the prescription of Kennicutt 1998 for $H\alpha$ and [O II]. Using the [O III] line to arrive at a SFR is less secure due to the effects of metallicity and gas temperature (Kennicutt et al. 2000, Kennicutt 1992). For eight of the ELGs in the sample, [O III] is the only line measured in the spectrum, and thus we use the [O III] SFR calibration from Straughn et al. (2009), which is derived from ELGs with both $H\alpha$ and [O III] in their spectra, and should be considered a lower limit. Figure 5 shows the SFR as a function of redshift for these galaxies, using $H\alpha$ when available; then [O II] and [O III] in order of preference. The detection limit is evident in this plot; we see the expected bias toward higher SFRs at higher redshifts.

The broad–band spectral energy distributions (SEDs), using ten band WFC3 and ACS data from 0.2–1.7 microns, were fit to a grid of models using the derived redshifts listed in Table 1, yielding galaxy stellar masses (Cohen et al., in preparation). These Bruzual & Charlot (2003) models were generated assuming an exponentially declining star formation history, and varying the time scale τ , internal extinction A_V , and age. The specific star–formation rates (sSFRs; line–calculated SFR per unit stellar mass) of these galaxies are

shown as a function of stellar mass in Figure 6, which is consistent with the general negative trend observed previously for galaxies at redshifts up to $z \simeq 2$ (e.g., Feulner et al. 2005, Bauer et al. 2005, Erb et al. 2006, Elbaz et al. 2007, Noeske et al. 2007, Rodighiero et al. 2010, etc.). Since our sample is selected based on the presence of emission lines (and thus ongoing star formation) we do not expect to see the galaxies with much lower SFRs which would likely occupy the lower-left area of Fig. 6 (detection limits also affect the selection of low-SFR galaxies). While the sample is clearly small due to the limited volume observed and we would likely miss any rare, high-mass, high-sSFR sources that might occupy the upper-right area of Figure 6, previous studies using large galaxy samples including Spitzer IRAC 3.6 micron data indicate that these sources are in fact not missed in these studies—i.e., that the upper limit to the galaxies’ SFR as a function of mass is real (Noeske et al. 2007).

In Figure 7 we show the sSFR as a function of redshift in different mass bins, which is consistent with previous studies showing the trend of lower sSFR for higher mass galaxies as a function of redshift (e.g., Zheng et al. 2007, Damen et al. 2009, Rodighiero et al. 2010). While these previous studies investigating the sSFR as a function of redshift have made use of very large samples of galaxies from an array of large observational programs (COMBO-17, Zheng et al. 2007; SIMPLE—Spitzer IRAC and MUSYC, Fazio et al. 2004, Damen et al. 2009; GOODS, Dickinson et al. 2003; see also Martin et al. 2007 and Perez-Gonzalez et al. 2008), we have demonstrated here that the WFC3 IR grism data generally reflect these trends using only two orbits of HST time. Future observations of this type will serve to investigate these preliminary trends in a more statistically significant way.

5. Summary

We detect a total of 73 emission lines from 48 galaxies in the ERS II grism field, allowing calculation of line fluxes, SFRs, and grism-spectroscopic redshifts. Thirteen of these galaxies had emission lines in the optical ACS G800L grism data and 35 are newly-detected star-forming galaxies with emission lines in the infrared. We show the SFRs of these galaxies as a function of redshift and discuss trends involving SFRs and galaxy masses and redshifts. These data are consistent with previous studies showing that the sSFRs of the most massive ($M > 10^{11} M_{\odot}$) star-forming galaxies are generally lower than their lower mass counterparts as a function of redshift (Zheng et al. 2007, Damen et al. 2009). These data demonstrate the efficiency of the WFC3 grisms in detecting faint star-forming galaxies at $z \simeq 0.2-2.5$. This work sets the stage for larger area and deeper studies of star-forming galaxies with WFC3 in the future, which will serve to greatly increase the sample size and statistics, and will probe even fainter and less massive sources.

This research was supported in part by an appointment to the NASA Postdoctoral Program at Goddard Space Flight Center, administered by Oak Ridge Associated Universities through a contract with NASA (ANS). This paper is based on Early Release Science observations made by the WFC3 Scientific Oversight Committee. We thank the anonymous referee for suggestions which improved the paper. We are grateful to the Director of the Space Telescope Science Institute for awarding Director’s Discretionary time for this program. Finally, we are deeply indebted to the brave astronauts of STS-125 for rejuvenating HST.

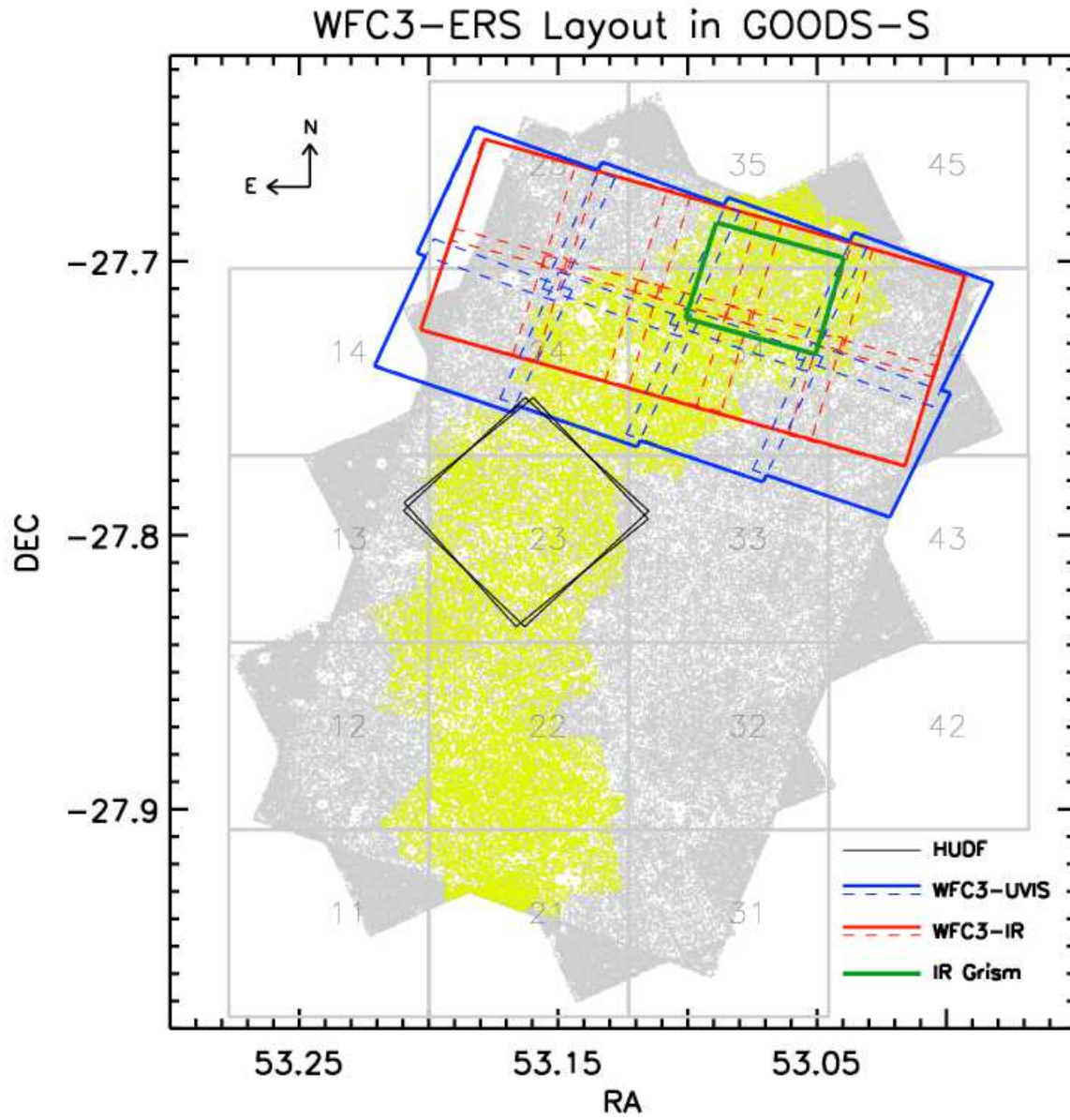


Fig. 1.— ERS II Layout in GOODS-South. Grey area is ACS GOODS-South with tile numbers for that dataset. Yellow areas are the five ACS PEARS grism fields; the black box is ACS HUDF. The WFC3 ERS II UVIS fields are outlined in blue, and WFC3 ERS II IR fields are outlined in red. The green box is the WFC3 ERS II IR grism field.

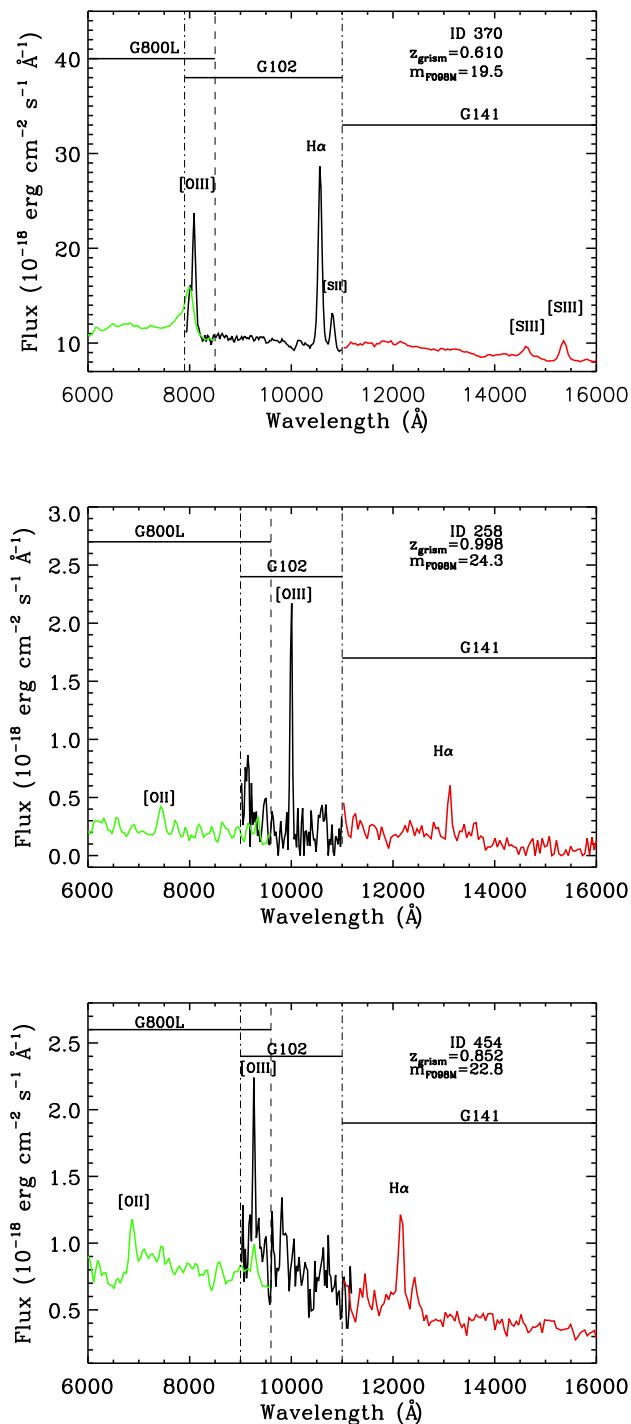


Fig. 2.— Three example grism spectra for ELGs (Table 1 Objects 370, 258, 454 from top to bottom) pre-selected from the ACS PEARS grism ELG study of Straughn et al. (2009). The ACS G800L data are shown in green; WFC3 G102 in black, and WFC3 G141 in red. The ACS G800L fluxes have been scaled for visual purposes to match the WFC3 data. Compared to ACS G800L, the higher-resolution WFC3 grisms allow detection of the [S II] and [S III] lines.

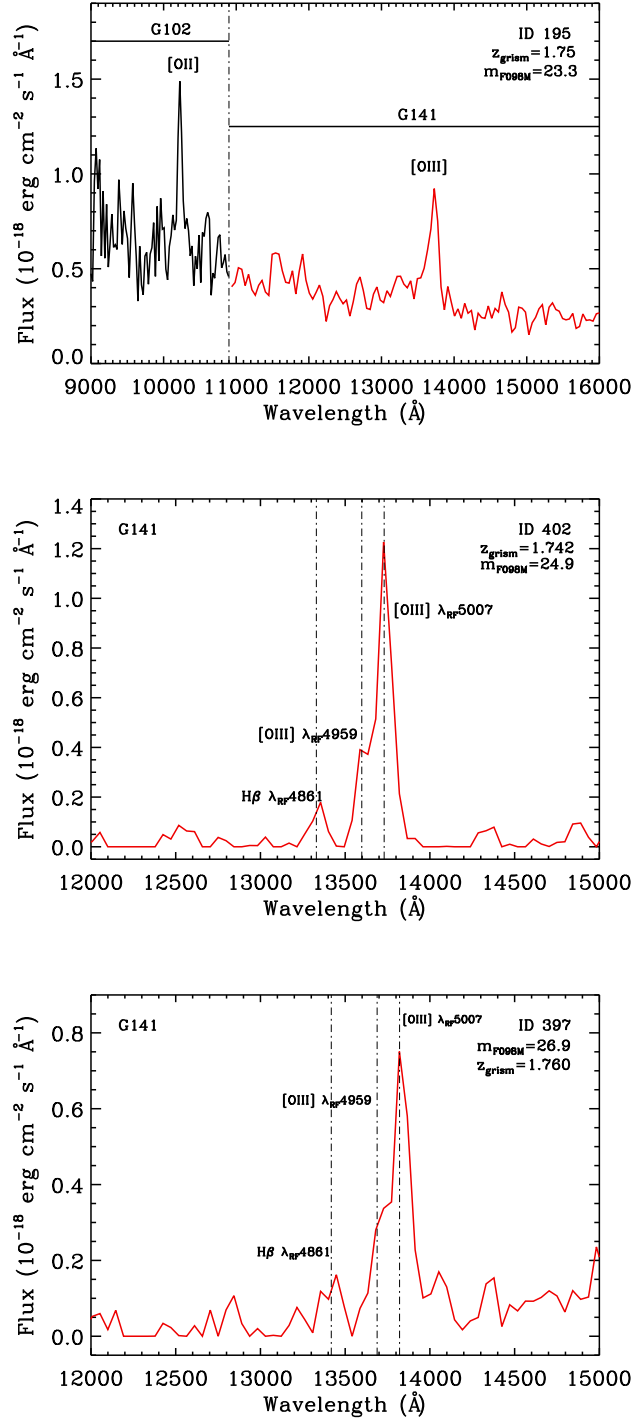


Fig. 3.— Three example grism spectra for ELGs with detected emission lines only in the IR grisms. Of note in the sample are intermediate redshift galaxies with extremely faint continuum fluxes and strong emission lines, as exemplified by Objects 402 and 397 here. The higher resolution of the WFC3 grisms allows detection of the two [O III] $\lambda\lambda 4959\text{\AA}$, 5007\AA lines (though not resolved) along with H β , providing a line identification for these faint sources with no previously-measured redshifts.

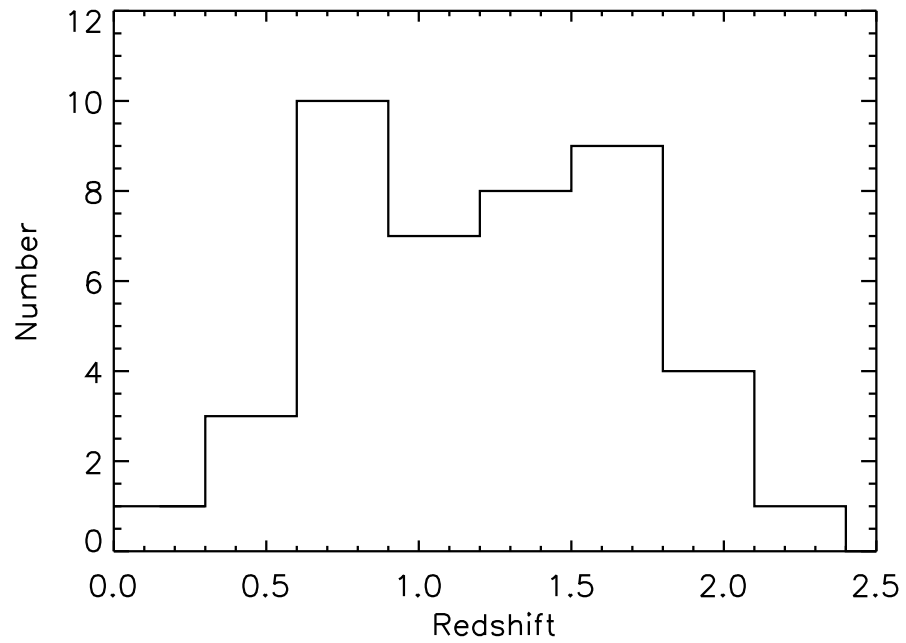


Fig. 4.— Grism–spectroscopic redshift distribution of WFC3 ELGs. The $H\alpha$, $[O\text{III}]$, and $[O\text{II}]$ emission lines are visible in the WFC3 grism bandpasses at redshifts $0.2 \lesssim z \lesssim 1.4$, $1.2 \lesssim z \lesssim 2.2$ and $2.0 \lesssim z \lesssim 3.3$ respectively. The majority of galaxies have more than one emission line, allowing secure line identifications and grism redshift determination.

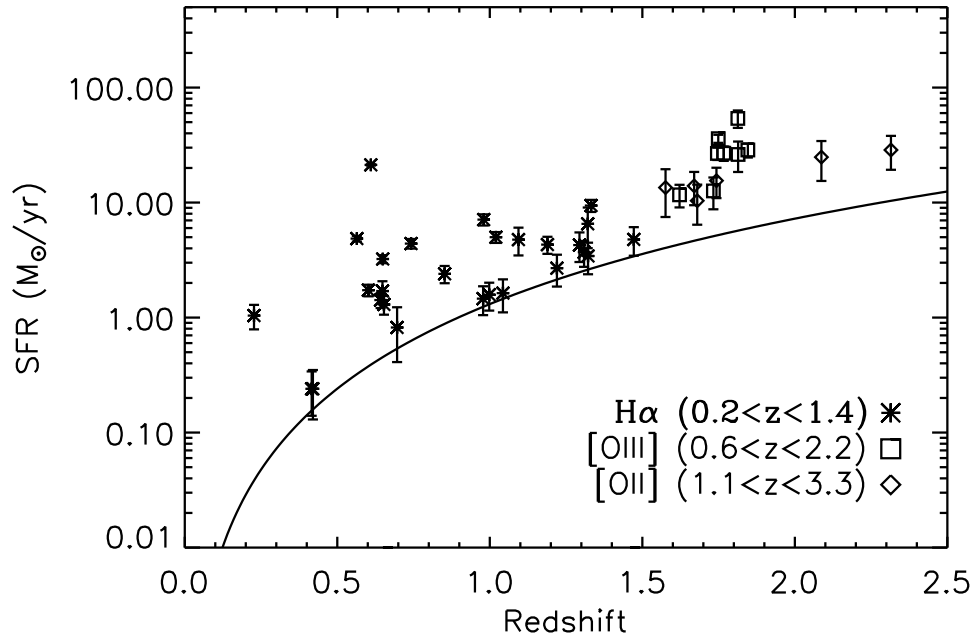


Fig. 5.— Star-formation rate for grism-detected sources as a function of redshift. SFRs are calculated from $H\alpha$, $[O\text{II}]$, and $[O\text{III}]$ line fluxes in order of preference, as described in Section 4.3.

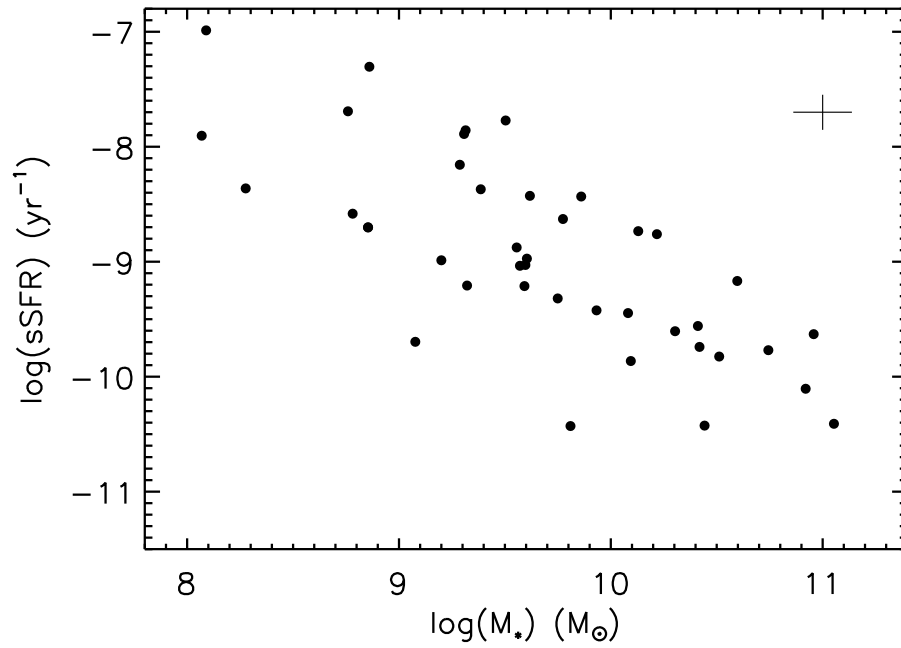


Fig. 6.— Specific star-formation rate as a function of stellar mass. The SFRs are computed by line flux measurements and the stellar masses are calculated from SED fits (Section 4.3). The results from the WFC3 IR grism data are consistent with previous studies showing the relation of lower sSFR at higher mass. Average error estimate for the sample is shown in the upper-right.

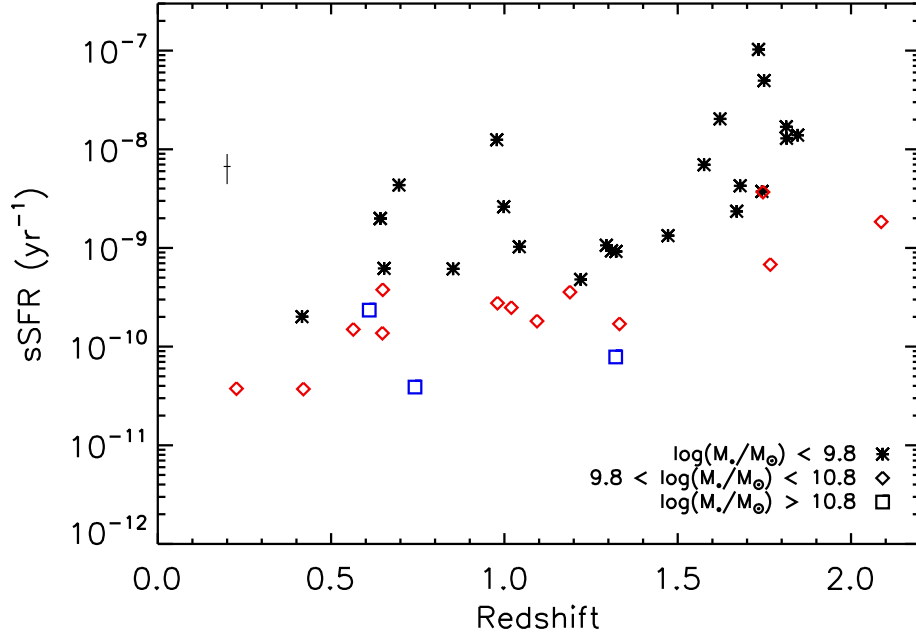


Fig. 7.— Specific star–formation rate as a function of redshift for three different mass bins. Although the sample size is small, the 2–orbit WFC3 grism data results are consistent with previous large survey studies that show the general trend of lower sSFRs for the highest mass galaxies as a function of redshift. Average error estimations are shown in upper–left. The lowest redshift source in the highest mass bin (blue squares) is an AGN, so some contribution to the line flux from the AGN is expected and likely results in a higher calculated SFR (uncorrected for AGN contamination).

Table 1. Global Properties of Emission-Line Galaxies

ID	RA (deg)	Dec (deg)	$AB(F098M)$ (mag)	Wavelength (Å)	Flux ($10^{-18} \text{ erg/s/cm}^2$)	EW (Å)	Line ID	SFR $M_{\odot} \text{ yr}^{-1}$	Grism Redshift	Flag –
432	53.0484200	-27.7095337	24.45	12850	94.7±18	114	[O III]	19.7±3	1.573	1
				9599	60.0±26	35	[O II]	13.5±6	1.573	1
499	53.0515862	-27.7047272	25.06	16226	44.5±12	199	H α	4.8±1	1.472	1
				12381	37.3±16	176	[O III]	6.7±2	1.472	1
370 [†]	53.0551300	-27.7113667	19.51	8080	1140.5±91	62	[O III]	23.7±1	0.610	1
				14620	166.6±16	22	[S III] λ 9069	–	–	1
				10810	344.9±22	35	[S II]	–	–	1
				10565	1733.6±23	98	H α	21.2±0	0.610	1
				15355	250.8±15	36	[S III] λ 9532	–	–	1
186	53.0555878	-27.7234249	23.23	11436	129.1±38	189	[O III]	16.5±4	1.294	1
				15056	54.7±15	81	H α	4.3±1	1.294	1
262	53.0558815	-27.7187843	25.63	13650	47.8±14	248	[O III]	12.6±3	1.733	3
226 [‡]	53.0558815	-27.7210884	24.04	13406	35.6±11	100	H α	1.6±0	1.043	1
				10229	99.5±31	110	[O III]	7.6±2	1.043	1
316	53.0565033	-27.7156715	23.33	13254	115.4±12	125	H α	5.0±0	1.020	2
238	53.0569191	-27.7202835	22.85	12453	–	–	[O III]	–	1.493	1
				16247	–	–	H α	–	1.476	1
				8682	259.9±48	59	[O III]	8.4±1	0.738	1
336 [†]	53.0577126	-27.7135887	20.71	15745	32.8±11	16	[S III] λ 9069	–	–	1
				11699	69.1±18	35	[S II]	–	–	1
				11430	222.4±21	62	H α	4.4±0	0.738	1
				16549	53.3±11	28	[S III] λ 9532	–	–	1
				13352	49.6±13	388	–	–	–	–
411	53.0586700	-27.7082272	25.84	13352	49.6±13	388	–	–	–	
				578	53.0589218	-27.6978111	24.33	16636	104.9±18	133
559	53.0613785	-27.6981163	22.15	12354	49.6±16	67	[O II]	28.6±9	2.315	1
				9317	47.8±21	21	H α	0.2±0	0.420	1
539	53.0624619	-27.6987267	25.04	15709	39.6±12	212	–	–	–	
103	53.0633392	-27.7272835	26.87	13397	61.0±17	121	[O III]	15.0±4	1.682	1
				9987	39.3±15	73	[O II]	10.4±3	1.682	1
427	53.0643387	-27.7056999	22.48	9294	48.4±21	31	H α	0.2±0	0.416	1
195	53.0656700	-27.7203941	23.34	13711	94.0±15	103	[O III]	25.3±4	1.745	1
				10224	53.7±15	19	[O II]	15.5±4	1.745	1
364	53.0693359	-27.7090893	23.52	10775	102.6±14	73	H α	1.4±0	0.642	1
				8219	376.6±98	270	[O III]	8.7±2	0.642	1

Table 1—Continued

ID	RA (deg)	Dec (deg)	$AB(F098M)$ (mag)	Wavelength (Å)	Flux ($10^{-18} \text{ erg/s/cm}^2$)	EW (Å)	Line ID	SFR $M_{\odot} \text{ yr}^{-1}$	Grism Redshift	Flag –
246	53.0700035	-27.7165890	24.95	8489	70.1±34	72	[O III]	2.0±0	0.696	1
				11133	48.7±23	273	H α	0.8±0	0.696	1
215	53.0703392	-27.7178669	23.46	10935	–	–	H α	–	0.666	1
563	53.0705452	-27.6956444	23.77	9949	53.8±17	36	[O II]	14.0±4	1.673	1
				13353	93.1±14	143	[O III]	22.6±3	1.673	1
402	53.0712967	-27.7058105	24.94	13730	133.0±10	656	[O III]	35.9±2	1.749	3
211 [†]	53.0714226	-27.7175884	20.41	10267	478.8±28	44	H α	4.9±0	0.564	1
476	53.0715446	-27.7006989	25.27	16555	67.8±10	353	–	–	–	–
193	53.0723381	-27.7186718	20.98	10813	119.6±25	27	H α	1.7±0	0.648	1
175	53.0725441	-27.7198391	24.38	12984	37.2±10	231	H α	1.5±0	0.978	3
583	53.0730896	-27.6939487	24.17	15239	41.7±12	225	H α	3.4±1	1.322	2
250	53.0734215	-27.7159519	22.03	10819	227.1±18	86	H α	3.2±0	0.649	2
210	53.0735054	-27.7173939	22.71	10845	90.0±16	34	H α	1.3±0	0.653	1
445	53.0736694	-27.7024498	23.22	14368	67.9±11	68	H α	4.3±0	1.189	2
566	53.0740471	-27.6945629	22.80	15303	112.4±13	73	H α	9.4±1	1.332	2
474	53.0740891	-27.7001171	24.31	13713	99.4±12	121	[O III]	26.7±3	1.746	1
454	53.0761719	-27.7011452	22.76	9264	59.2±16	40	[O III]	2.7±0	0.852	1
				12157	86.1±14	88	H α	2.4±0	0.852	1
251	53.0767975	-27.7144222	25.20	14213	92.9±13	162	[O III]	28.6±4	1.846	3
397	53.0772133	-27.7047558	26.86	13821	96.9±13	254	[O III]	26.9±3	1.760	1
263	53.0772972	-27.7131157	23.88	14569	39.8±12	82	H α	2.7±0	1.222	1
				11097	27.0±12	24	[O III]	3.0±1	1.222	1
339	53.0773392	-27.7081985	22.65	8002	863.9±163	375	[O III]	16.9±3	0.602	1
				10512	145.8±17	83	H α	1.7±0	0.602	1
265	53.0780029	-27.7129498	25.34	13775	42.5±12	182	–	–	–	–
351	53.0785751	-27.7074108	22.62	13744	92.2±25	97	H α	4.8±1	1.094	2
498	53.0789223	-27.6977272	21.52	12996	181.0±20	77	H α	7.1±0	0.980	3
512	53.0792542	-27.6968098	25.15	13097	52.0±11	301	[O III]	11.7±2	1.622	1
10	53.0816612	-27.6881046	22.72	15232	79.5±30	59	H α	6.5±2	1.321	3
242	53.0821304	-27.7137547	24.61	11506	55.3±21	97	[O II]	24.8±9	2.070	1
				15337	62.9±14	111	[O III]	25.7±5	2.070	1
3 [†]	53.0825462	-27.6896439	18.67	8054	858.4±203	40	H α	1.0±0	0.227	1
418	53.0848389	-27.7014771	24.92	14051	182.6±31	344	[O III]	53.9±9	1.813	3
437	53.0855865	-27.6999226	24.70	14053	88.6±26	501	[O III]	26.2±7	1.814	3

REFERENCES

- Atek, H. et al. 2010, *ApJ*, 723, 104
- Balestra, I. et al. 2010, *A&A*, 512, A12
- Bauer, A.E., Drory, N., & Feulner, G. 2005, *ApJL*, 621, 89
- Beckwith, S.V.W. et al. 2006, *AJ*, 132, 1729
- Bertin, E. & Arnouts, S. 1996, *A&AS*, 117, 363
- Bruzual, G. & Charlot, S. 2003, *MNRAS* 344, 1000
- Bouwens, R.J. et al. 2010a, *ApJL*, 709
- 2010b, *ApJL*, 708, 69
- Damen, M., Labb, I., Franx, M., van Dokkum, P. G., Taylor, E. N., Gawiser, E. J. 2009, *ApJ*, 690, 937
- Dickinson, M., et al. 2003, *Proc. ESO/USM Workshop, “The Mass in Galaxies at Low and High Redshift”*, ed. R. Bender, & A. Renzini (Berlin: Springer), 324
- Fazio, G. G., et al. 2004, *ApJS*, 154, 10
- Feulner, G., Goranova, Y., Drory, N., Hopp, U., & Bender, R. 2005, *MNRAS*, 358, L1
- Finkelstein, S.L. et al. 2010, *ApJ*, 719, 1250
- Gallego, J., Zamorano, J., Aragon-Salamanca, A., & Rego, M. 1995, *ApJ* 455, L1
- Gardner, J.P., et al. 2006, *SSR*, 123, 485
- Giavalisco, M. et al. 2004, *ApJL*, 600, 93
- Grazian, A., et al. 2006, *A&A* 449, 951
- Grogin, N.A., Malhotra, S., Rhoads, J., Cohen, S., Hathi, N., Windhorst, R., Pirzkal, N. 2007, *BAAS*, 211, 4605
- Hathi, N.P., et al. 2010, *ApJ*, 720, 1708
- Kennicutt, R.C., Jr. 1983, *ApJ* 272, 54
- 1992, *ApJ*, 388, 310

Table 1—Continued

ID	RA (deg)	Dec (deg)	$AB(F098M)$ (mag)	Wavelength (Å)	Flux ($10^{-18} \text{ erg/s/cm}^2$)	EW (Å)	Line ID	SFR $M_{\odot} \text{ yr}^{-1}$	Grism Redshift	Flag –
258	53.0857124	-27.7113400	24.32	9998	115.9±31	65	[O III]	7.9±2	0.998	1
				13111	38.4±10	99	H α	1.6±0	0.998	1
416	53.0860062	-27.7011986	24.26	12760	163.7±34	567	–	–	–	–
146	53.0872955	-27.7184486	24.44	11539	50.2±24	159	[O III]	6.7±3	1.309	1
				15156	46.1±11	138	H α	3.7±0	1.309	1

*NOTE: No data in the case of fluxes (and EW, SFR) indicates that the spectrum had a high level of contamination but wavelengths were secure enough to warrant redshift determination. In the case of line IDs, no data indicates that no suitable line ID was found for the given input redshift. “Grism Redshift” column gives re-calculated redshift based on the line identification. “Flag” column gives source of input redshift used for line identification, where used: 1—two lines visible in spectrum, no prior redshift needed; 2—single line in spectrum, line ID and grism redshift based on prior spectroscopic redshift; 3—single line in spectrum, line ID and grism redshift based on prior photometric redshift.

†CDF-S X-ray sources identified as AGN by Szokoly et al. 2004.

‡New spectroscopic redshift (no previous photometric or spectroscopic redshift measurements).

- 1998, *ARA&A* 36, 189
- Kennicutt, R.C., Jr., Bresolin, F., French, H., & Martin, P. 2000, *ApJ*, 537, 589
- Kewley, L.J., Geller, M.J., Jansen, R.A. 2004, *AJ*, 127, 2002
- Koekemoer, A. M., Fruchter, A. S., Hook, R. N., & Hack, W. 2002, *The 2002 HST Calibration Workshop*, ed. S. Arribas, A. Koekemoer, and B. Whitmore (Baltimore:STScI), 337
- Kümmel, M., Walsh, J. R., Pirzkal, N., Kuntschner, H., & Pasquali, A. 2009, *PASP*, 121, 59
- H. Kuntschner, H. Bushouse, M. Kümmel, J. R. Walsh 2009a, *ST-ECF ISR WFC3-2009-18 WFC3 SMOV proposal 11552: Calibration of the G102 grism*
- 2009b, *ST-ECF ISR WFC3-2009-17 WFC3 SMOV proposal 11552: Calibration of the G141 grism*
- Labbe, I. et al. 2010, *ApJL*, 716, 103
- Larson, R.B. & Tinsley, B.M. 1978, *ApJ* 219, 46
- Li et al. 2008, *MNRAS*, 385, 1903L
- Martin, D. C., et al. 2007, *ApJS*, 173, 415
- McCarthy, P.J., et al. 1999, *ApJ*, 520, 548
- McLure, R. J., Dunlop, J. S., Cirasuolo, M., Koekemoer, A. M., Sabbi, E., Stark, D. P., Targett, T. A., Ellis, R. S. 2010, *MNRAS*, 403, 960
- Meurer et al. 2007, *AJ*, 134, 77
- Navarro, J., Frenk, C., & White, S. 1997, *ApJ*, 490, 493
- Noeske, K. et al. 2007, *ApJL*, 660, 43
- Oesch, P. A., Bouwens, R. J., Carollo, C. M., Illingworth, G. D., Trenti, M., Stiavelli, M., Magee, D., Labb, I., Franx, M. 2010, *ApJL*, 709, 21
- Overzier, R.A. et al. 2008, *ApJ*, 677, 37
- Perez-Gonzalez, P. G., et al. 2008, *ApJ*, 675, 234
- 2006, *ApJ* 636, 582
- Rodighiero, G. et al. 2010, *A&A*, 518, L25

- Rosa, M., Joubert, M., Benvenuti, P. 1984, *A&AS*, 57, 361
- Straughn, A.N. et al. 2008, *AJ*, 135, 1624
- Straughn, A.N. et al. 2009, *AJ*, 138, 1022
- Szokoly, G.P. et al. 2004, *ApJS*, 155, 271
- van Dokkum, P.G & Brammer, G. 2010, arXiv:1003:3446
- White, S. D. M., & Frenk, C. S. 1991, *ApJ*, 379, 52
- Wilkins, S. M., Bunker, A. J., Ellis, R. S., Stark, D., Stanway, E. R., Chiu, K., Lorenzoni, S., Jarvis, M. J. 2010, *MNRAS*, 403, 938
- Windhorst, R.A. et al. 2010, submitted, arXiv:1005.2776
- Vanzella, E. et al. 2008, *A&A*, 478, 83V
- Wuyts, S., Labbe, I., Schreiber, N. M. F., et al. 2008, *ApJ*, 682, 985
- Xia, L. et al. 2010, submitted
- Xu, C., et al. 2007, *AJ* 134, 169
- Yan, H. Windhorst, R.A., Hathi, N.P., Cohen, S.H., Ryan, R.E., O’Connell, R., McCarthy, P.J. 2010a, *RAA*, 10, 867
- Yan, H. et al. 2010b, *ApJ*, submitted
- Yan, L., McCarthy, P.J., Freudling, W., Teplitz, H.I., Malumuth, E.M., Weymann, R.J., & Malkan, M.A. 1999, *ApJL* 519, L47
- Zheng, X. Z., Bell, E. F., Papovich, C., Wolf, C., Meisenheimer, K., Rix, H.-W., Rieke, G, & Somerville, R. 2007, *ApJ*, 661, 41